

Electric-Field-Induced Coherent Control of Nitrogen-Vacancy Centers

Gerald Q. Yan,¹ Senlei Li,¹ Tatsuya Yamamoto², Mengqi Huang,¹ Nathan J. McLaughlin,¹ Takayuki Nozaki², Hailong Wang,³ Shinji Yuasa², and Chunhui Rita Du^{1,3,*}

¹*Department of Physics, University of California, San Diego, La Jolla, California 92093, USA*
²*National Institute of Advanced Industrial Science and Technology (AIST), Research Center for Emerging Computing Technologies, Tsukuba, Ibaraki 305-8568, Japan*

³*Center for Memory and Recording Research, University of California, San Diego, La Jolla, California 92093-0401, USA*



(Received 24 January 2022; revised 16 June 2022; accepted 14 November 2022; published 12 December 2022)

Enabling scalable and energy-efficient control of spin defects in solid-state media is desirable for realizing transformative quantum information technologies. Exploiting voltage-controlled magnetic anisotropy, we report the coherent manipulation of nitrogen-vacancy ($N\text{-}V$) centers by spatially confined magnetic stray fields produced by a proximate resonant magnetic tunnel junction (MTJ). Remarkably, the coherent coupling between $N\text{-}V$ centers and the MTJ can be systematically controlled by a dc bias voltage, allowing for appreciable electrical tunability in the presented hybrid system. In comparison with current state-of-the-art techniques, the demonstrated $N\text{-}V$ -based quantum operational platform exhibits significant advantages in scalability, device compatibility, and energy efficiency, further expanding the role of $N\text{-}V$ centers in a broad range of quantum computing, sensing, and communications applications.

DOI: [10.1103/PhysRevApplied.18.064031](https://doi.org/10.1103/PhysRevApplied.18.064031)

Over the past decade, nitrogen-vacancy ($N\text{-}V$) centers, which are optically active spin defects in diamond with single-spin addressability, excellent quantum coherence, and remarkable functionality over a broad range of temperatures, have emerged as a promising platform for developing transformative quantum information science and technology [1–3]. $N\text{-}V$ centers have already been successfully applied to quantum sensing [2–4], imaging [5–8], communication [9–11], and network research [10–12], enabling high field sensitivity, nanoscale spatial resolution, and long-range qubit transmission. Hybrid systems establishing strong coupling between $N\text{-}V$ centers, photons, and other solid-state media for applications in functional quantum devices are also currently being developed [13–31].

Despite significant progress in developing optical entanglement and optimizing spin-coherence times [9–12], problems related to scalability, qubit density, and local qubit control remain to be solved to fully realize the potential of $N\text{-}V$ centers for developing alternative quantum processors [16,30,32–34]. In the current state of the art, the quantum spin state of $N\text{-}V$ centers is typically manipulated by spatially dispersive Oersted fields generated by radio-frequency (rf) electric currents [35,36], imposing an inherent challenge for achieving highly local

and scalable manipulation of $N\text{-}V$ centers. In addition, the current-induced Joule heating inherent to this approach can generate thermal noise, resulting in potential issues for developing $N\text{-}V$ -based quantum processors consisting of multiple qubits in one diamond [37,38]. These long-standing issues have thus far hindered the development of $N\text{-}V$ -based quantum computing platforms and proven profoundly difficult to overcome.

To address this challenge, we integrate $N\text{-}V$ centers with a functional magnetic-tunnel-junction (MTJ) device exhibiting voltage-controlled magnetic anisotropy (VCMA) [39–41], enabling electric-field-driven coherent control of $N\text{-}V$ centers in an energy-efficient manner. Manipulation of the spin qubits is achieved by exploiting the spatially confined magnetic stray fields produced by a resonant magnetic free layer within the MTJ stack. It is worth noting that the millisecond-long $N\text{-}V$ spin-relaxation times (T_1) are preserved in the presented hybrid system, offering an attractive platform for developing high-density scalable $N\text{-}V$ -based solid-state architectures for applications at the forefront of quantum science and technologies.

We first describe the detailed structure of the device used in our measurements, as illustrated in Fig. 1(a). A MTJ composed of (from bottom to top) Ta(5 nm)/Co₄₀Fe₄₀B₂₀(1 nm)/MgO(2 nm)/Co₅₆Fe₂₄B₂₀(5 nm)/Ru(7 nm)/Cr(5 nm)/Au(50 nm) is fabricated on a Si substrate (see Appendix A for details). The in-plane magnetized Co₅₆Fe₂₄B₂₀ serves as a fixed reference layer,

*c1du@physics.ucsd.edu

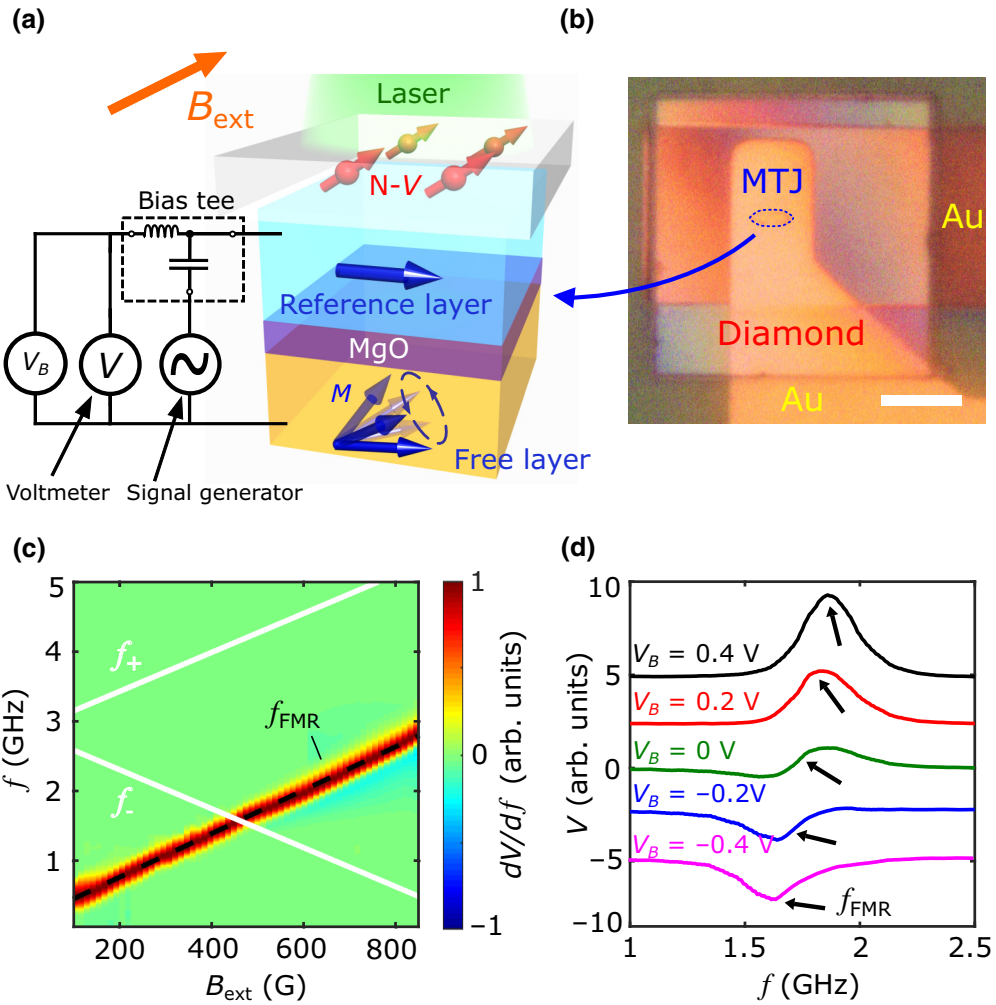


FIG. 1. (a) Schematic illustration of an N-V MTJ hybrid device. Diamond microchip containing N-V ensembles is placed on top of a prepared MTJ. N-V spin state is optically addressed using confocal or widefield microscopy. Electrical excitation and detection of VCMA-induced magnetic resonance utilizes a standard homodyne detection circuit. (b) Optical image showing the prepared N-V MTJ device. Blue dashed line outlines the edges of the MTJ, and the scale bar is 10 μm . (c) Derivative of measured dc voltage, dV/df , as a function of external magnetic field, B_{ext} , and frequency, f , of the applied voltage. White lines represent the field-dependent upper and lower N-V electron-spin-resonance frequencies, f_{\pm} . Black dashed line represents the fitting using a modified Kittel equation. (d) Dc-bias-voltage-induced variation of spectrum shape and shift of the resonant frequency, f_{FMR} , of a MTJ device measured at $B_{\text{ext}} = 490$ G.

while $\text{Co}_{40}\text{Fe}_{40}\text{B}_{20}$ forms the free layer with spontaneous perpendicular magnetization due to a weak out-of-plane anisotropy [42–46]. Viewed from above, the MTJ has an elongated hexagonal shape with a length of 6 μm and a width of 2 μm . A diamond microchip [7] with lateral dimensions of $30 \times 30 \mu\text{m}^2$ is placed on top of the MTJ. N-V centers are shallowly implanted on the bottom surface of the diamond chip with a density of about 1500 per μm^2 , and the distance between the N-V centers and the top surface of the MTJ stack is estimated to be about 200 nm. The optical image shown in Fig. 1(b) provides an overview of the prepared device. In our experiments, N-V centers are optically addressed using either confocal or widefield microscopy [6,47–49]. To enable

coherent control of the N-V centers, we take advantage of the oscillating magnetic stray fields generated by the proximate resonant MTJ. Applying a voltage across the MTJ modifies the electron charge or spin densities at the $\text{Co}_{40}\text{Fe}_{40}\text{B}_{20}/\text{MgO}$ interface and induces a variation of the magnetic anisotropy in the free layer through the spin-orbit interaction [41,50–53]. Due to the VCMA, the magnetic easy axis varies between the out-of-plane and in-plane directions, depending on the sign and magnitude of the applied voltage. Therefore, applying a rf voltage to the MTJ can excite coherent magnetic oscillations of the $\text{Co}_{40}\text{Fe}_{40}\text{B}_{20}$ free layer under an appropriate static external magnetic field, where the magnetic sample is driven under resonant conditions.

The experimental measurements of VCMA-driven ferromagnetic resonance (FMR) of the MTJ using a homodyne detection technique [39] are shown in Fig. 1(a). An external magnetic field, B_{ext} , is applied at an angle of 54° relative to the out-of-plane direction, in alignment with the corresponding N-V axis. The in-plane projection of B_{ext} lies along the long axis of the MTJ, and a rf voltage with a power of -2 dBm is applied across the MTJ via the rf input port of a bias tee. Under FMR conditions, the oscillating tunnel magnetoresistance of the MTJ couples with the rf tunnel current to produce a significant dc voltage, V , which can be detected through the dc port of the bias tee. In this way, an output dc voltage is measured as a function of input frequency. Figure 1(c) plots a two-dimensional (2D) map of the derivative of the measured dc voltage with respect to frequency as a function of B_{ext} and frequency, f , of the applied rf voltage. VCMA-induced FMR is observed with expected field and frequency dependence, in accordance with theoretical predictions (see Appendix A for details). The FMR dispersion curve intersects with the N-V electron-spin-resonance (ESR) frequency at a field

of $B_{\text{ext}}=447 \text{ G}$ and frequency of $f=1.62 \text{ GHz}$. Under a fixed external magnetic field, $B_{\text{ext}}=490 \text{ G}$, the resonant frequency of the MTJ can be tuned with VCMA by varying the dc bias voltage across the device, as shown in Fig. 1(d).

Next, we utilize confocal microscopy (see Appendix B for details) to perform Rabi oscillation measurements of N-V centers located in an area of about $1 \times 1 \mu\text{m}^2$ of the diamond that is directly above the MTJ, demonstrating electric-field-driven coherent control of N-V centers. Before discussing the experimental details, we first briefly review the pertinent physical properties of N-V centers. A N-V center consists of a substitutional nitrogen atom adjacent to a carbon-atom vacancy in one of the nearest-neighboring sites of a diamond crystal lattice [1–3]. The negatively charged N-V state has an $S=1$ electron spin in the ground state and serves as a three-level system. When an oscillating magnetic field at the N-V site, the N-V occupation probabilities will periodically oscillate between two different spin levels. These are referred to as Rabi oscillations [1–3] and are illustrated in Fig. 2(a). Here, f_{\pm} denote the N-V ESR

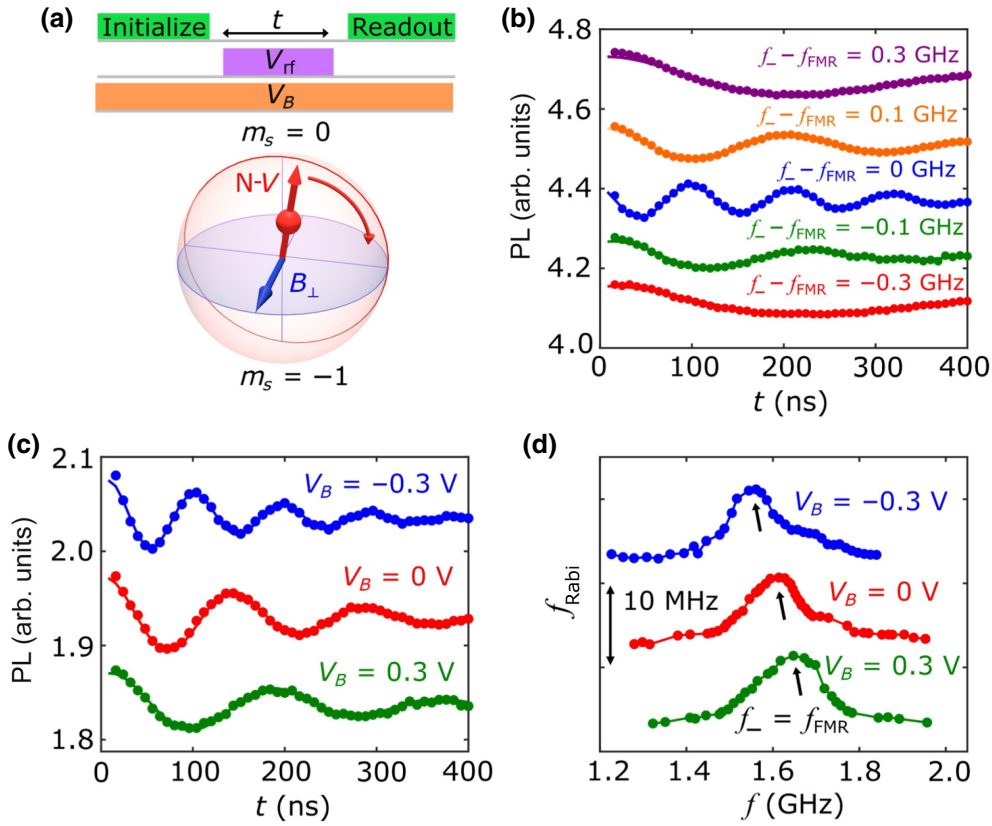


FIG. 2. (a) Top panel, optical and rf voltage pulse sequence used in the N-V Rabi oscillation measurements. Bottom panel, schematic of N-V Rabi oscillations between $m_s=0$ and $m_s=-1$ states on the Bloch sphere. (b) N-V photoluminescence (PL) intensity as a function of delay time, t , measured at detuning frequencies ($f_{\perp}-f_{\text{FMR}}$) of ± 0.3 , ± 0.1 , and 0 GHz . (c) Time-dependent N-V PL spectra measured with the application of dc bias voltages, V_B , of -0.3 , 0 , and 0.3 V under an external magnetic field, $B_{\text{ext}}=470 \text{ G}$. Rabi oscillation frequency is enhanced or suppressed, depending on the sign of the dc bias voltage. (d) Measured Rabi frequency as a function of N-V ESR frequency, f_{\perp} , under three different dc bias voltages. Curves are vertically offset for visual clarity.

frequencies corresponding to the spin transition between the $m_s = 0$ and $m_s = \pm 1$ states. Our N-V Rabi oscillation measurements are performed under N-V ESR conditions, and detuning is defined as the difference between the N-V ESR frequency and the resonant frequency, f_{FMR} , of the magnetic junction device. The top panel of Fig. 2(a) shows the specific measurement protocol. A 3- μs -long green-laser pulse is first applied to initialize the N-V centers to the $m_s = 0$ state. Next, a rf voltage pulse at the N-V ESR frequencies is applied to excite the FMR of the MTJ. When the resonant frequency, f_{FMR} , matches f_{\pm} , oscillating stray fields generated by the MTJ will enhance the rate of the $m_s = 0 \leftrightarrow \pm 1$ N-V spin transitions. Lastly, a second green-laser pulse is applied to read out the N-V spin state via the spin-dependent photoluminescence (PL). The duration, t , of the rf voltage pulse is systematically varied to probe the time-dependent variation of the N-V PL. A dc bias voltage is also applied during the above measurements, providing electrical tunability of the coherent N-V-magnet coupling.

Figure 2(b) shows measured N-V Rabi oscillation spectra as a function of t at different N-V ESR frequencies. When f_- is detuned from the resonant frequency, f_{FMR} , of the MTJ such that $|f_- - f_{\text{FMR}}| \geq 0.3$ GHz, the measured PL spectrum is essentially independent of the duration of the rf voltage pulse, indicating negligible N-V-magnet coupling. As f_- approaches f_{FMR} , the measured PL spectra exhibit characteristic periodic oscillations with a Rabi frequency, f_{Rabi} , of approximately 5 MHz at a detuning of ± 0.1 GHz. Remarkably, when $f_- = f_{\text{FMR}}$, we observe significantly faster oscillatory behavior of the N-V PL spectrum with an enhanced f_{Rabi} of about 10 MHz, demonstrating robust electric-field-induced coherent control of N-V spin states. The dramatic enhancement of the N-V spin-rotation rate is driven by phase synchronization between the resonant MTJ and proximate N-V centers. The Rabi oscillation frequency is proportional to the magnitude of the local magnetic stray field, B_{\perp} , transverse to the N-V spin orientation at the N-V site and is calculated to be 4.8 G, in agreement with theoretical calculations (see Appendix C for details). By applying a dc bias voltage, V_B , to vary the resonant frequency, f_{FMR} , we are able to further achieve effective tuning of the N-V Rabi oscillation frequency through electric-field-induced variation of the static magnetic anisotropy [54,55], as shown in Fig. 2(c). Figure 2(d) plots the measured f_{Rabi} as a function of f_- for three different dc bias voltages. f_{FMR} shifts towards higher (lower) frequencies with positive (negative) V_B , due to a decrease (increase) of the perpendicular magnetic anisotropy. Peak values of f_{Rabi} are consistently observed when f_- matches f_{FMR} , demonstrating that the coherent N-V spin rotation is indeed driven by VCMA-induced FMR of the MTJ.

We next utilize widefield magnetometry (see Appendix B for details) to further illustrate the presented N-V control scheme and its electrical tunability. The laser-beam-spot

width used in the widefield measurements is approximately $30 \times 30 \mu\text{m}^2$, allowing simultaneous imaging of all the N-V centers in the diamond microchip that are positioned above the MTJ device. The N-V fluorescence is captured using a CMOS camera. Figures 3(a)–3(e) show a representative series of 2D widefield images of the measured N-V Rabi oscillation rate at five detuning frequencies ($f_- - f_{\text{FMR}}$), corresponding to points “A”–“E” shown in Fig. 3(f). At $f_- = 1.49$ GHz [Fig. 3(a)], the measured N-V Rabi oscillation frequency, f_{Rabi} , is nearly negligible over the entire measured area due to a significant mismatch between the N-V ESR frequency and MTJ resonant frequency. Moderate N-V spin rotation emerges when $f_- = 1.57$ GHz [Fig. 3(b)], suggesting the establishment of dipole-mediated coherent coupling between the resonant MTJ and N-V centers. The coupling strength is maximized when f_- matches f_{FMR} , leading to the highest Rabi oscillation frequencies of the N-V centers directly above the MTJ [Fig. 3(c)]. Further increasing f_- results in detuning of the N-V center and VCMA FMR frequencies and subsequent suppression of the Rabi oscillation frequencies, as illustrated in Figs. 3(d) and 3(e). Note that the inhomogeneous distribution of the Rabi frequencies over the device indicates a spatially nonuniform distribution of the magnetic stray-field magnitudes produced by the MTJ, which can be tied to underlying magnetic inhomogeneities and domains in the device. Next, we consider the potential advantages of the presented N-V-based quantum operational platform. In contrast with conventional N-V-control schemes using spatially dispersive Oersted fields generated by rf currents, the N-V MTJ hybrid device utilizes magnetic stray fields, which are more spatially confined due to dipole-dipole interactions, to enable coherent control of N-V centers. To better illustrate this point, Fig. 3(g) shows one-dimensional profiles of the local magnetic stray field, B_{\perp} (transverse to the N-V axis), measured across the short axis of the MTJ at three N-V ESR frequencies. Notably, B_{\perp} shows a finite value at positions within the width of the MTJ device. At positions beyond the width of the device, B_{\perp} quickly decays to a vanishingly small value on a length scale of about 100 nm. Our experimental results agree with theoretical calculations (see Appendix D for details), confirming the highly localized N-V control strategy demonstrated by the presented N-V MTJ device. This merit is particularly beneficial for the development of high-density N-V-based information-processing and -storage technologies, where minimal crosstalk between neighboring operational units is desirable [19,56,57]. The solid-state nature of the MTJ devices and N-V centers renders them readily compatible with a large family of functional quantum architectures, promoting the use of N-V centers in implementing large-scale integrated quantum networks [11]. The voltage-controlled coherent N-V-magnet coupling is further illustrated in Figs. 4(a)–4(c). At $B_{\text{ext}} = 460$ G and $f_- = 1.58$ GHz, application of a negative bias voltage of

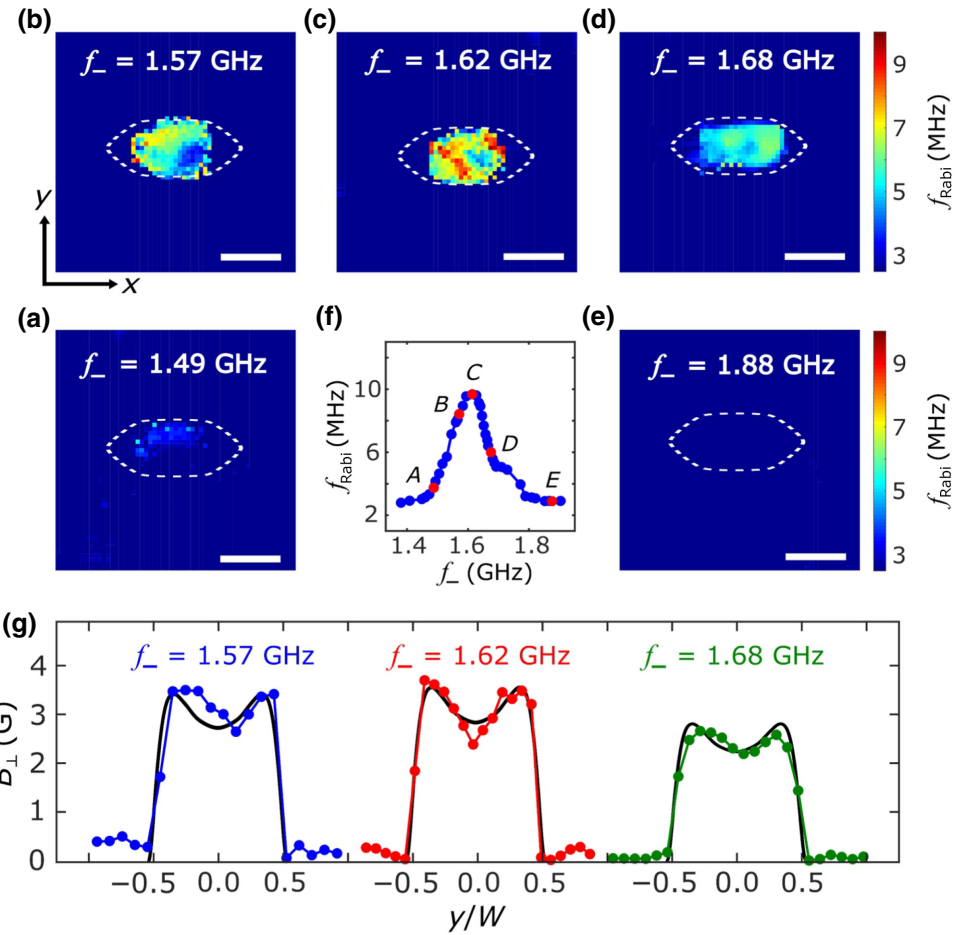


FIG. 3. (a)–(e) 2D maps of the Rabi oscillation frequency measured at N-V ESR frequencies, f_- , of 1.49, 1.57, 1.62, 1.68, and 1.88 GHz, respectively. White dashed line outlines the lateral boundary of the MTJ underneath the diamond chip, and the scale bar is $2 \mu\text{m}$. (f) Rabi oscillation frequency, f_{Rabi} , measured as a function of the ESR frequency, f_- , for N-V centers directly above the center of the MTJ. Points “A”–“E” marked on the curve correspond to the five N-V ESR frequencies, f_- , used in the N-V widefield magnetometry measurements presented in (a)–(e). (g) Line cuts of extracted magnetic stray field, B_\perp (transverse to the N-V axis), along the short axis (y axis) of the MTJ at ESR frequencies of 1.57, 1.62, and 1.68 GHz. Micromagnetic simulation results (black curves) are in qualitative agreement with experimental data. Unit of the y axis is normalized by the short-axis width ($W=2 \mu\text{m}$) of the MTJ device.

-0.4 V significantly enhances the coherent N-V rotation rate [Fig. 4(a)], while a positive voltage effectively suppresses the N-V Rabi frequencies [Fig. 4(c)]. Our results demonstrate that the coherent N-V–magnet coupling can be electrically switched *on* and *off* by a moderate bias voltage. We expect that further optimization of the material and device parameters could add appreciable tunability of the N-V MTJ hybrid device across a broad range of experimental conditions.

Lastly, we perform N-V spin-relaxometry measurements using confocal microscopy to ascertain the spin-relaxation times (T_1) of the N-V centers directly above the MTJ. Our measurements are performed at $B_{\text{ext}}=438$ G and $f_- = 1.64$ GHz. At $V_B=0$ V, f_- is close to f_{FMR} , which is the minimum frequency of the magnon band. Application of a dc bias voltage shifts f_{FMR} higher or lower

than f_- , depending on the sign of the voltage, as illustrated in Fig. 4(d). The top panel of Fig. 4(e) shows the optical and rf sequence used in the N-V relaxometry measurements. A green-laser pulse is first applied to initialize the N-V spins to the $m_s=0$ state. After a delay time, t , we measure the occupation probabilities of the $m_s=-1$ states by applying a rf π voltage pulse at the corresponding ESR frequencies and measure the spin-dependent PL with a green-laser read-out pulse. Note that the rf pulses are delivered with a rf voltage applied across the MTJ. The bottom panel of Fig. 4(e) plots the measured N-V PL as a function of delay time t at three different bias voltages. By fitting the results with an exponential decay function, $P(t)=A_0+Ae^{-t/T_1}$ [36,58], where $P(t)$ is the measured photoluminescence, and A and A_0 are constants; the T_1 time of the N-V centers is measured to be 1429, 588, and

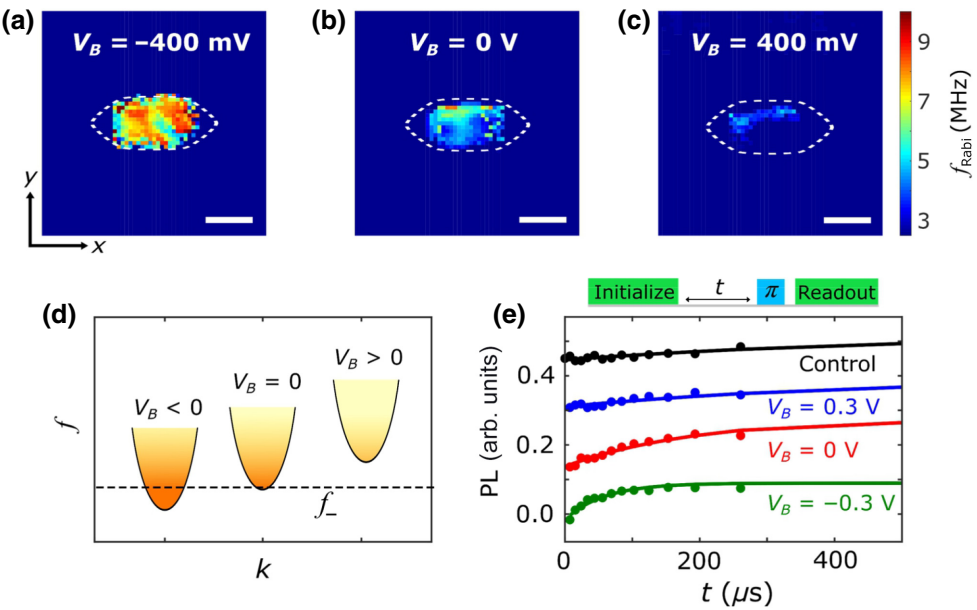


FIG. 4. (a)–(c) 2D maps of Rabi oscillation frequency, f_{Rabi} , measured at $f_- = 1.58$ GHz with a bias voltage of -0.4 , 0 , and $+0.4$ V, respectively, under an external magnetic field, $B_{\text{ext}} = 460$ G. White dashed line outlines the lateral boundary of the MTJ, and the scale bar is $2 \mu\text{m}$. (d) Schematic showing the magnon dispersions for various bias voltages and their intersection with the N-V ESR frequency, f_- . Magnon occupation of the magnetic free layer follows the Bose-Einstein distribution, as indicated by fading color intensities. Positive (negative) bias shifts the magnon band upwards (downwards) relative to f_- . Dispersion are shifted in k for visual clarity. (e) Top panel, optical and rf voltage pulse sequence used in the N-V relaxometry measurements. Bottom panel, N-VPL intensity measured as a function of delay time t , from which the N-V relaxation time, T_1 , is extracted to be 1429 , 588 , and $175 \mu\text{s}$ under the application of dc bias voltages of 0.3 , 0 , and -0.3 V, respectively. Control measurements of N-V centers in the diamond microchip give $T_1 = 1667 \mu\text{s}$.

$175 \mu\text{s}$ for bias voltages, V_B , of $+0.3$, 0 , and -0.3 V, respectively. The electrical tunability of T_1 exploits the voltage-controlled f_{FMR} of the magnetic free layer, which determines the magnitude of spin noise at the N-V ESR frequency, f_- , and leads to relaxation of the N-V center spins [36]. Note that T_1 of N-V centers with f_- tuned slightly above the magnon band ($V_B > 0$ V) is comparable to the intrinsic relaxation time of N-V centers positioned away from the MTJ ($T_1 = 1667 \mu\text{s}$), which is slightly shorter than the value reported in Ref. [37]. In the future, it would also be valuable to characterize the coherence time of N-V centers in the hybrid system.

In summary, we demonstrate coherent control of N-V centers by a resonant MTJ. Exploiting VCMA-driven oscillating stray fields, we achieve local control and electrically tunable control of N-V centers, offering opportunities for developing scalable high-density N-V-based quantum operational units. Due to the large electrical resistance of the insulating tunnel layer of the device, the magnitude of the rf electric current flowing through the MTJ is in the microampere regime, virtually eliminating ohmic losses and the resulting thermal decoherence of nearby N-V centers. We note that the millisecond-long spin-relaxation time (T_1) remains preserved in N-V centers positioned in nanoscale proximity to the MTJ. These merits highlight the

presented hybrid solid-state system as a promising building block for a broad range of transformative applications in N-V-based quantum computing, sensing, and networking [5,11,16,28,56,57,59,60].

ACKNOWLEDGMENTS

The authors would like to thank Hanyi Lu for assistance in sample preparation. The authors thank Yaroslav Tserkovnyak, Ilya N. Krivorotov, Pramey Upadhyaya, and Avinash Rustagi for insightful discussions. G.Q.Y., S.L., M.H., and C.R.D. are supported by the U.S. National Science Foundation (NSF) under Grants No. ECCS-2029558 and No. DMR-2046227. N.J.M., H.W., and C.R.D. acknowledge support from the Air Force Office of Scientific Research under Grant No. FA9550-20-1-0319 and its Young Investigator Program under Grant No. FA9550-21-1-0125.

APPENDIX A: EXTENDED CHARACTERIZATION RESULTS OF MAGNETIC-TUNNEL-JUNCTION DEVICES

The MTJ devices used in this study are prepared by standard photolithography, dry etching, sputtering, and lift-off processes. Details of the nanofabrication have been

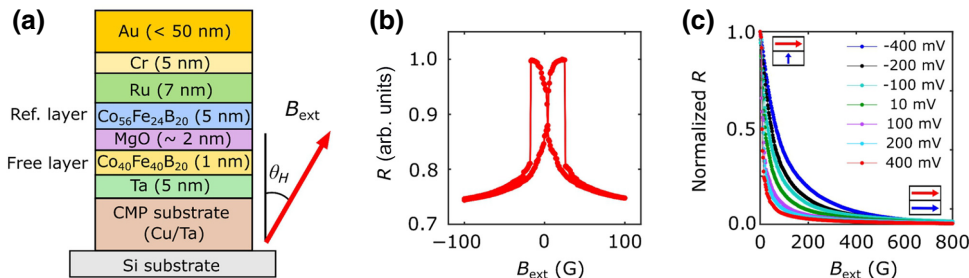


FIG. 5. (a) Cross-section schematic of a MTJ. (b) Tunnel magnetoresistance, R , measured with an in-plane magnetic field applied parallel to the long axis of the junction device. (c) Normalized tunnel magnetoresistance, R , measured with different dc bias voltages. Insets illustrate the magnetic configurations of the reference layer (red arrow) and free layer (blue arrow) in the high- and low-field regimes.

reported in previous work [39]. Figure 5(a) shows the composition of a MTJ device. The Co₅₆Fe₂₄B₂₀ reference layer is in-plane magnetized, while the Co₄₀Fe₄₀B₂₀ free layer exhibits spontaneous perpendicular magnetization due to weak out-of-plane anisotropy. The resistance-area product of a tunnel junction is about 63 kΩ μm². For dc electrical transport characterization, an in-plane magnetic field is applied along the long axis of the pillar junction, a dc electric voltage of 10 mV is applied across the junction, and the tunnel resistance is measured by using a nanovoltmeter. Figure 5(b) shows the field dependence of the measured tunnel magnetoresistance of a junction device. In the low-field regime, the reference and free-layer magnetizations tend to orient perpendicular to each other, leading to a high tunnel magnetoresistance. When the applied magnetic field is large enough to overcome the anisotropy of the free layer, the reference and free-layer magnetizations align parallel with each other, as illustrated in the inset of Fig. 5(c), resulting in a low-resistance state of the junction device. We measure the tunnel magnetoresistance of the junction under different dc bias voltages to evaluate the effects of the VCMA. When a voltage is applied across the junction, modification of the charge or spin densities at the Co₄₀Fe₄₀B₂₀/MgO interface will induce a variation of the magnetic anisotropy of the Co₄₀Fe₄₀B₂₀ free layer through the spin-orbit interaction [50–54]. The out-of-plane anisotropy is enhanced or suppressed, depending on the sign of the dc bias voltage. Figure 5(c) shows the in-plane field dependence of the normalized tunnel

magnetoresistance measured under a series of bias voltages. The measured tunnel magnetoresistance decreases with increasing in-plane magnetic field. The saturation field of the tunnel magnetoresistance corresponding to the perpendicular anisotropy of the free layer can be electrically controlled, confirming the VCMA effect discussed above.

When applying a rf voltage across the junction, the VCMA can cause periodic magnetic oscillations of the Co₄₀Fe₄₀B₂₀ free layer under certain static external-magnetic-field conditions. The precessional magnetization induces a time-dependent oscillating tunnel magnetoresistance, which couples with the tunnel current to produce a significant dc voltage. We use a standard homodyne detection technique to detect VCMA-driven FMR [39]. For these measurements, the external magnetic field, B_{ext} , is applied at an angle of 54° relative to the out-of-plane direction, and the in-plane projection of B_{ext} is directed along the long axis of the junction device. Figure 6(a) shows the frequency dependence of measured homodyne detection signals under different external magnetic fields. Clear anti-Lorentzian features are observed under FMR conditions, which systematically shift towards higher frequencies as B_{ext} is increased. We fit the spectra with the sum of a symmetric Lorentzian and an asymmetric anti-Lorentzian function to determine the resonant frequency, f_{FMR} . Figure 6(b) plots the obtained f_{FMR} as a function of B_{ext} , which can be expressed using a modified Kittel formula [39]:

$$f_{\text{FMR}} = \frac{\gamma}{2\pi} \sqrt{\{B_{\text{ex}} - B_{d,\text{eff}} \cos^2 \theta_H + B_{d,\text{in-plane}}\} \{B_{\text{ex}} - B_{d,\text{eff}} \cos(2\theta_H)\}}, \quad (\text{A1})$$

where $\gamma/2\pi = 2.9 \times 10^6$ (s⁻¹ G⁻¹) for the Co₄₀Fe₄₀B₂₀ free layer, $B_{d,\text{eff}}$ is the effective demagnetization field along the out-of-plane direction, $\theta_H = 54^\circ$, and $B_{d,\text{in-plane}}$ is the

difference between in-plane demagnetization fields along the short- and long-axis directions. Using numerical fitting, $B_{d,\text{eff}}$ and $B_{d,\text{in-plane}}$ of the Co₄₀Fe₄₀B₂₀ free layer are

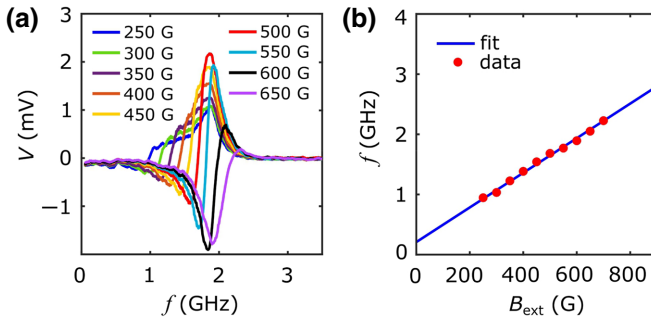


FIG. 6. (a) Homodyne detection dc signals, V , measured as a function of the frequency, f , of the applied voltage under different external magnetic fields. Input rf power is -2 dBm. Characteristic anti-Lorentzian features are observed at the resonance conditions of a MTJ. (b) Measured resonant frequency (red points) of the junction device as a function of the applied external magnetic field. Measured data agree well with the modified Kittle equation (blue curve).

evaluated to be about 256 and 168 G, respectively. In general, we expect that experimental control of f_{FMR} across a broad frequency range is achievable by tuning the external field and intrinsic magnetic properties of the samples.

APPENDIX B: NITROGEN-VACANCY MEASUREMENTS

$N\text{-}V$ measurements are performed using confocal and widefield microscopy. For $N\text{-}V$ confocal measurements, the green-laser pulses used for $N\text{-}V$ initialization and read-out are generated by an acoustic optical modulator in a double-pass configuration. The laser power entering the objective is approximately 0.5 mW. The $N\text{-}V$ spin states are optically addressed by measuring the PL from a green read-out pulse via an avalanche photodiode. The trigger pulses to the optical modulator and photon counter are generated by a programmable pulse generator. Microwave voltages are supplied by a Stanford Research SG386 signal generator and modulated by a microwave switch

(Minicircuits ZASWA-2-50DR+) before being delivered to the MTJ device.

For $N\text{-}V$ widefield measurements, the green-laser pulses used for $N\text{-}V$ initialization and read-out are generated by an electrically driven 515-nm laser with an output power of 10 mW. The laser-beam spot after passing the objective has an area of about $26 \times 26 \mu\text{m}^2$ and is focused onto the diamond microchip positioned on top of the magnetic device. $N\text{-}V$ fluorescence is captured using a CMOS camera. The pulses used to drive the green laser and to trigger the camera exposures are generated by a programmable pulse generator. The external magnetic field for the $N\text{-}V$ measurements is generated by a permanent cylindrical Nd-Fe-B magnet attached to a three-axis motorized translational stage. The $N\text{-}V$ density of the used diamond microchip is estimated using algorithm analysis of $N\text{-}V$ photoluminescence images. A brief description of this method can be found in the literature [61]. The $N\text{-}V$ implantation depth is estimated to be about 10 nm using the implantation energy (6 keV) and stopping and range of ions in matter simulations. Note that the magnetic reference layer of the junction device is premagnetized before our $N\text{-}V$ measurements.

APPENDIX C: EXPERIMENTAL MEASUREMENTS OF LOCAL OSCILLATING MAGNETIC STRAY FIELDS BY $N\text{-}V$ RABI OSCILLATIONS

When the FMR frequency, f_{FMR} , of the MTJ matches the $N\text{-}V$ ESR frequency, the oscillating magnetic fields generated by the resonant junction drive periodic oscillations of the proximate $N\text{-}V$ spins between two different spin states in the rotation frame, which are referred to as Rabi oscillations. The magnitude of the oscillating magnetic stray fields transverse to $N\text{-}V$ axis can be extracted from the $N\text{-}V$ Rabi oscillation frequency, f_{Rabi} , as follows [62]:

$$B_{\perp} = \frac{2\sqrt{2}\pi f_{\text{Rabi}}}{\gamma}, \quad (\text{C1})$$

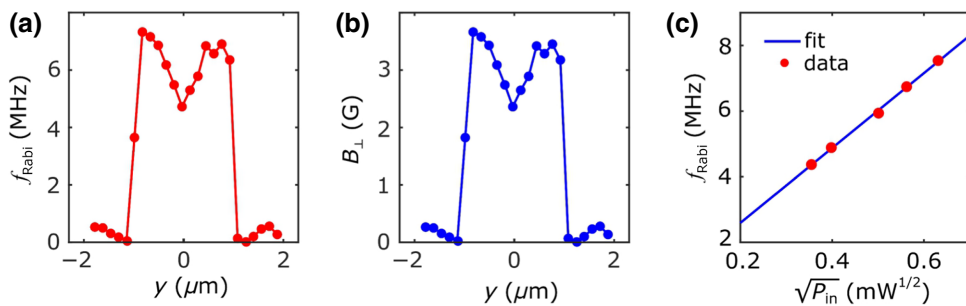


FIG. 7. (a) Measured $N\text{-}V$ Rabi oscillation frequency at different points along the short axis (y axis) of a MTJ device. (b) Extracted spatially dependent (along the short axis) magnetic stray field, B_{\perp} , perpendicular to the $N\text{-}V$ spin orientation. (c) Measured $N\text{-}V$ Rabi oscillation frequency, f_{Rabi} (red points), shows a linear dependence on square root of the input rf power, $\sqrt{P_{\text{in}}}$.

where $\gamma/2\pi = 2.8$ MHz/G is the electron-spin gyromagnetic ratio. Figure 7(a) shows the Rabi oscillation frequency measured at several points along the short axis (y axis) of a tunnel-junction device. Using Eq. (C1), we can obtain the spatial variation of B_{\perp} , as shown in Fig. 7(b), which agrees with the theoretical calculations discussed Appendix D. We note that the measured N-V Rabi oscillation frequency, f_{Rabi} , driven by the resonant MTJ exhibits a linear dependence on the square root of the input microwave power, $\sqrt{P_{\text{in}}}$, as shown in Fig. 7(c). This is expected because the magnetic stray field, B_{\perp} , is proportional to the precessional cone angle of the resonant free layer, which increases linearly with $\sqrt{P_{\text{in}}}$.

APPENDIX D: THEORETICAL CALCULATIONS OF OSCILLATING MAGNETIC STRAY FIELDS GENERATED BY VCMA-DRIVEN FMR

In this section, we present the method used to calculate the amplitudes of the oscillating magnetic stray fields generated by the VCMA-driven FMR. Figure 8(a) shows the schematic of a junction device consisting of a reference layer and free layer separated by an insulating tunnel layer. The lateral dimensions of the junction are 6 and 2 μm along the long and short axes, which are parallel to the x and y axes, respectively. The thicknesses of the free and reference layers are 1 and 5 nm, respectively. We assume that the free layer occupies the space, Ω , with

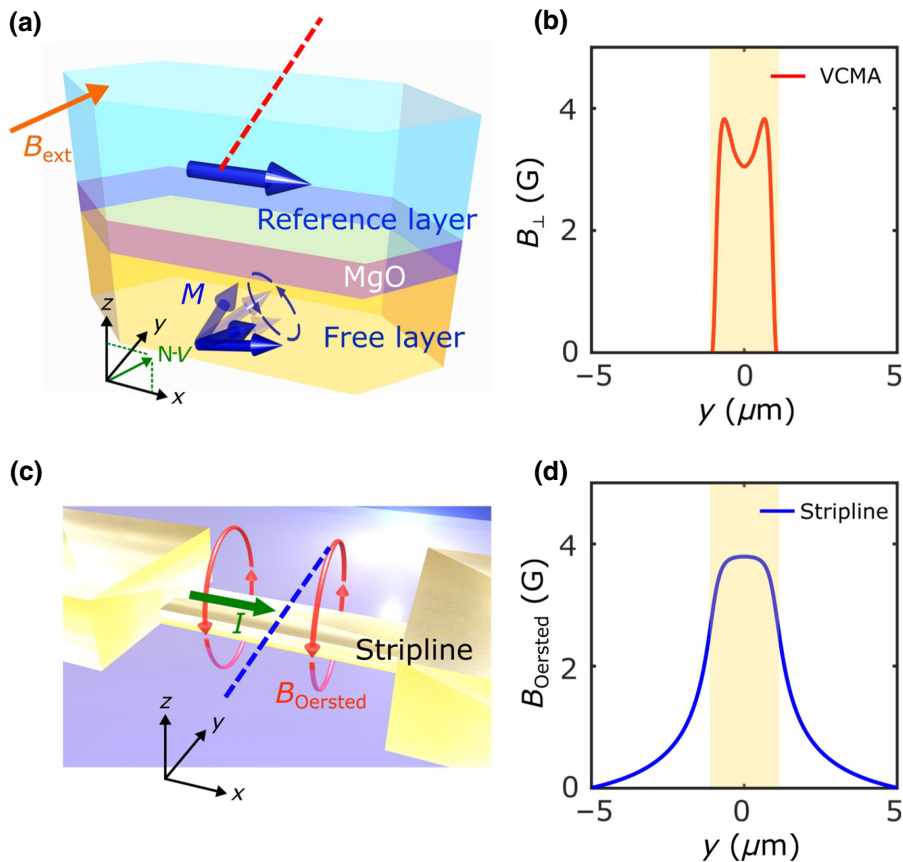


FIG. 8. (a) Schematic of a MTJ device composed of the reference, tunnel, and free layers. The red dashed line 300 nm above the free layer ($x = 0, z = 300\text{ nm}$) represents the linecut along which the spatially dependent magnetic stray field B_{\perp} generated by the resonant free layer is calculated. The N-V orientation is along $[\sin(54^{\circ}), 0, \cos(54^{\circ})]$ as illustrated. (b) Calculated one-dimensional spatially dependent magnetic stray field B_{\perp} (red line) along the linecut ($x = 0$ and $z = 300\text{ nm}$). The yellow shaded area represents the lateral length scale of the magnetic pillar junction along y axis. (c) Schematic of Oersted field B_{Oersted} generated by rf currents flowing in a 2- μm -wide Au stripline. The blue dashed line 300 nm above the stripline ($x = 0, z = 300\text{ nm}$) represents the linecut along which the spatially dependent Oersted field B_{Oersted} is calculated. The long and short axes of the stripline are parallel with the x and y axes, respectively, and the N-V orientation is the same as that shown in (a). (d) Calculated one-dimensional spatially dependent Oersted field B_{Oersted} (blue line) along the linecut ($x = 0$ and $z = 300\text{ nm}$), which is more spatially dispersive in comparison with the magnetic stray field generated from the resonant junction device (b). The yellow shaded area represents the lateral length of the Au stripline along the y axis.

$-3 \mu\text{m} \leq x \leq 3 \mu\text{m}$, $-1 \mu\text{m} \leq y \leq 1 \mu\text{m}$, $-1 \text{ nm} \leq z \leq 0$, and its surface lies in the x - y plane. N- V centers are contained in a diamond chip positioned on top of the junction device. The vertical distance between the N- V s and the surface of the free layer is 300 nm. An external magnetic field, B_{ext} , is applied along the N- V orientation direction: $\mathbf{e}_{\text{N}-V} = [\sin(54^\circ), 0, \cos(54^\circ)]$. In our calculations, we assume that the static magnetization of the reference layer lies along the x axis, and the static magnetization of the free layer is parallel to the external field direction. The saturation magnetization, $4\pi M_s$, of the free layer is about 15 kG [63]. When a rf voltage is applied across the junction, the dynamic magnetization, \mathbf{M} , of the free layer will precess around the equilibrium position, as illustrated by the blue dashed arrows in Fig. 8(a). The magnetic stray field, $\mathbf{B}_s(\mathbf{r}, t)$, at a location \mathbf{r} generated by the time-dependent magnetization distribution, $\mathbf{M}(\mathbf{r}', t)$, at location \mathbf{r}' of the free layer can be expressed as [64]

$$\mathbf{B}_s(\mathbf{r}, t) = \int \left\{ \frac{3(\mathbf{r} - \mathbf{r}')[\mathbf{M}(\mathbf{r}', t) \cdot (\mathbf{r} - \mathbf{r}')] }{|\mathbf{r} - \mathbf{r}'|^5} - \frac{\mathbf{M}(\mathbf{r}', t)}{|\mathbf{r} - \mathbf{r}'|^3} \right\} d^3 \mathbf{r}'. \quad (\text{D1})$$

Here, we are mainly interested in the transverse component, B_\perp (relative to the N- V axis), of the oscillating magnetic stray field along a line cut 300 nm above the free layer ($x = 0$ and $z = 300 \text{ nm}$). B_\perp is defined as $[B_{\max}(\mathbf{r}) - B_{\min}(\mathbf{r})]/2$, where $B_{\max}(\mathbf{r})$ and $B_{\min}(\mathbf{r})$ are the maximum and minimum values, respectively, of the time-dependent magnetic stray fields perpendicular to the N- V axis, $\mathbf{e}_{\text{N}-V} \times \mathbf{B}_s(\mathbf{r}, t)$. Figure 8(b) shows B_\perp calculated along the line cut across the junction device illustrated by the red dashed line ($x = 0$ and $z = 300 \text{ nm}$) shown in Fig. 8(a). At positions along the line for which $|y| \leq 1 \mu\text{m}$ (corresponding to the dimension along the short axis of the junction device), B_\perp exhibits a finite value as large as about 4 G. Outside this region, where $|y| > 1 \mu\text{m}$, the calculated magnetic stray field, B_\perp , exhibits a sharp decay and quickly reaches a vanishingly small value on a length scale of about 100 nm. We highlight that the magnetic stray fields generated from the VCMA-driven FMR are spatially more confined in comparison with the conventional Oersted field, B_{Oersted} , generated by microwave currents flowing in a 2- μm -wide Au stripline, as shown in Figs. 8(c) and 8(d). This can be understood qualitatively by considering the Biot-Savart law and magnetic dipole interactions, where B_{Oersted} and B_\perp spatially decay as $1/|r - r'|$ and $1/|r - r'|^3$, respectively. The “localized” magnetic stray fields generated by resonant MTJs provide opportunities for developing high-density N- V quantum spin processors with minimal mutual interference between neighboring operational units.

- [1] M. W. Doherty, N. B. Manson, P. Delaney, F. Jelezko, J. Wrachtrup, and L. C. L. Hollenberg, The nitrogen-vacancy colour centre in diamond, *Phys. Rep.* **528**, 1 (2013).
- [2] L. Rondin, J.-P. Tetienne, T. Hingant, J.-F. Roch, P. Maletinsky, and V. Jacques, Magnetometry with nitrogen-vacancy defects in diamond, *Rep. Prog. Phys.* **77**, 056503 (2014).
- [3] C. L. Degen, F. Reinhard, and P. Cappellaro, Quantum sensing, *Rev. Mod. Phys.* **89**, 035002 (2017).
- [4] M. Lesik, T. Plisson, L. Toraille, J. Renaud, F. Occelli, M. Schmidt, O. Salord, A. Delobbe, T. Debuisschert, L. Rondin, *et al.*, Magnetic measurements on micrometer-sized samples under high pressure using designed NV centers, *Science* **366**, 1359 (2019).
- [5] A. Finco, A. Haykal, R. Tanos, F. Fabre, S. Chouaieb, W. Akhtar, I. Robert-Philip, W. Legrand, F. Ajejas, K. Bouzehouane, *et al.*, Imaging non-collinear antiferromagnetic textures via single spin relaxometry, *Nat. Commun.* **12**, 767 (2021).
- [6] J.-P. Tetienne, N. Dotschuk, D. A. Broadway, A. Stacey, D. A. Simpson, and L. C. L. Hollenberg, Quantum imaging of current flow in graphene, *Sci. Adv.* **3**, e1602429 (2017).
- [7] Y. Schlussel, T. Lenz, D. Rohner, Y. Bar-Haim, L. Bougas, D. Groswasser, M. Kieschnick, E. Rozenberg, L. Thiel, A. Waxman, *et al.*, Wide-Field Imaging of Superconductor Vortices with Electron Spins in Diamond, *Phys. Rev. Appl.* **10**, 034032 (2018).
- [8] L. Thiel, Z. Wang, M. A. Tschudin, D. Rohner, I. Gutiérrez-Lezama, N. Ubrig, M. Gibertini, E. Giannini, A. F. Morpurgo, and P. Maletinsky, Probing magnetism in 2D materials at the nanoscale with single-spin microscopy, *Science* **364**, 973 (2019).
- [9] B. Hensen, H. Bernien, A. E. Dréau, A. Reiserer, N. Kalb, M. S. Blok, J. Ruitenberg, R. F. L. Vermeulen, R. N. Schouten, C. Abellán, *et al.*, Loophole-free Bell inequality violation using electron spins separated by 1.3 kilometres, *Nature* **526**, 682 (2015).
- [10] M. Pompili, S. L. N. Hermans, S. Baier, H. K. C. Beukers, P. C. Humphreys, R. N. Schouten, R. F. L. Vermeulen, M. J. Tiggelman, L. S. Martins, B. Dirkse, *et al.*, Realization of a multinode quantum network of remote solid-state qubits, *Science* **372**, 259 (2021).
- [11] M. Ruf, N. H. Wan, H. Choi, D. Englund, and R. Hanson, Quantum networks based on color centers in diamond, *J. Appl. Phys.* **130**, 070901 (2021).
- [12] C. E. Bradley, J. Randall, M. H. Abobeih, R. C. Berrevoets, M. J. Degen, M. A. Bakker, M. Markham, D. J. Twitchen, and T. H. Taminiau, A Ten-Qubit Solid-State Spin Register with Quantum Memory up to One Minute, *Phys. Rev. X* **9**, 031045 (2019).
- [13] A. Barfuss, J. Teissier, E. Neu, A. Nunnenkamp, and P. Maletinsky, Strong mechanical driving of a single electron spin, *Nat. Phys.* **11**, 820 (2015).
- [14] E. R. MacQuarrie, T. A. Gosavi, N. R. Jungwirth, S. A. Bhave, and G. D. Fuchs, Mechanical Spin Control of Nitrogen-Vacancy Centers in Diamond, *Phys. Rev. Lett.* **111**, 227602 (2013).
- [15] P. Rabl, S. J. Kolkowitz, F. H. L. Koppens, J. G. E. Harris, P. Zoller, and M. D. Lukin, A quantum spin transducer based on nanoelectromechanical resonator arrays, *Nat. Phys.* **6**, 602 (2010).

- [16] B. Flebus and Y. Tserkovnyak, Entangling distant spin qubits via a magnetic domain wall, *Phys. Rev. B* **99**, 140403 (2019).
- [17] D. Labanowski, V. P. Bhalla, Q. Guo, C. M. Purser, B. A. McCullian, P. C. Hammel, and S. Salahuddin, Voltage-driven, local, and efficient excitation of nitrogen-vacancy centers in diamond, *Sci. Adv.* **4**, eaat6574 (2018).
- [18] P. Andrich, C. F. de las Casas, X. Liu, H. L. Bretscher, J. R. Berman, F. J. Heremans, P. F. Nealey, and D. D. Awschalom, Long-range spin wave mediated control of defect qubits in nanodiamonds, *npj Quantum Inf.* **3**, 28 (2017).
- [19] M. Fukami, D. R. Candido, D. D. Awschalom, and M. E. Flatté, Opportunities for Long-Range Magnon-Mediated Entanglement of Spin Qubits via *On*- and *Off*-Resonant Coupling, *PRX Quantum* **2**, 040314 (2021).
- [20] A. B. Solanki, S. I. Bogdanov, A. Rustagi, N. R. Dilley, T. Shen, M. M. Rahman, W. Tong, P. Debasish, Z. Chen, J. Appenzeller, *et al.*, Electric field control of interaction between magnons and quantum spin defects, *Phys. Rev. Res.* **4**, L012025 (2022).
- [21] D. Prananto, Y. Kainuma, K. Hayashi, N. Mizuuchi, K. Uchida, and T. An, Probing Thermal Magnon Current Mediated by Coherent Magnon via Nitrogen-Vacancy Centers in Diamond, *Phys. Rev. Appl.* **16**, 064058 (2021).
- [22] M. S. Wolf, R. Badea, and J. Berezovsky, Fast nanoscale addressability of nitrogen-vacancy spins via coupling to a dynamic ferromagnetic vortex, *Nat. Commun.* **7**, 11584 (2016).
- [23] D. Lee, K. W. Lee, J. V. Cady, P. Ovartchaiyapong, and A. C. B. Jayich, Topical review: Spins and mechanics in diamond, *J. Opt.* **19**, 033001 (2017).
- [24] A. Solyom, Z. Flansberry, M. A. Tschudin, N. Leitao, M. Pioro-Ladrière, J. C. Sankey, and L. I. Childress, Probing a spin transfer controlled magnetic nanowire with a single nitrogen-vacancy spin in bulk diamond, *Nano Lett.* **18**, 6494 (2018).
- [25] Y. Hirayama, K. Ishibashi, and K. Nemoto, *Hybrid Quantum Systems* (Springer, Singapore, 2021).
- [26] X. Wang, Y. Xiao, C. Liu, E. L. Wong, N. J. McLaughlin, H. Wang, M. Wu, H. Wang, E. E. Fullerton, and C. R. Du, Electrical control of coherent spin rotation of a single-spin qubit, *npj Quantum Inf.* **6**, 78 (2020).
- [27] D. Kikuchi, D. Prananto, K. Hayashi, A. Laraoui, N. Mizuuchi, M. Hatano, E. Saitoh, Y. Kim, C. A. Meriles, and T. An, Long-distance excitation of nitrogen-vacancy centers in diamond via surface spin waves, *Appl. Phys. Express* **10**, 103004 (2017).
- [28] D. D. Awschalom, *et al.*, Quantum engineering with hybrid magnonics systems and materials, *IEEE Trans. Quantum Eng.* **2**, 1 (2021).
- [29] J. Trimble, B. Gould, F. J. Heremans, S. S.-L. Zhang, D. D. Awschalom, and J. Berezovsky, Relaxation of a single defect spin by the low-frequency gyroscopic mode of a magnetic vortex, *J. Appl. Phys.* **130**, 083903 (2021).
- [30] L. Trifunovic, F. L. Pedrocchi, and D. Loss, Long-Distance Entanglement of Spin Qubits via Ferromagnet, *Phys. Rev. X* **3**, 041023 (2013).
- [31] H. Zhang, M. J. H. Ku, F. Casola, C. H. R. Du, T. van der Sar, M. C. Onbasli, C. A. Ross, Y. Tserkovnyak, A. Yacoby, and R. L. Walsworth, Spin-torque oscillation in a magnetic insulator probed by a single-spin sensor, *Phys. Rev. B* **102**, 024404 (2020).
- [32] F. Dolde, I. Jakobi, B. Naydenov, N. Zhao, S. Pezzagna, C. Trautmann, J. Meijer, P. Neumann, F. Jelezko, and J. Wrachtrup, Room-temperature entanglement between single defect spins in diamond, *Nat. Phys.* **9**, 139 (2013).
- [33] A. Cooper, W. K. C. Sun, J.-C. Jaskula, and P. Cappellaro, Identification and Control of Electron-Nuclear Spin Defects in Diamond, *Phys. Rev. Lett.* **124**, 083602 (2020).
- [34] N. Y. Yao, L. Jiang, A. V. Gorshkov, P. C. Maurer, G. Giedke, J. I. Cirac, and M. D. Lukin, Scalable architecture for a room temperature solid-state quantum information processor, *Nat. Commun.* **3**, 800 (2012).
- [35] G. D. Fuchs, V. V. Dobrovitski, D. M. Toyli, F. J. Heremans, and D. D. Awschalom, Gigahertz dynamics of a strongly driven single quantum spin, *Science* **326**, 1520 (2009).
- [36] C. Du, T. van der Sar, T. X. Zhou, P. Upadhyaya, F. Casola, H. Zhang, M. C. Onbasli, C. A. Ross, R. L. Walsworth, Y. Tserkovnyak, and A. Yacoby, Control and local measurement of the spin chemical potential in a magnetic insulator, *Science* **357**, 195 (2017).
- [37] A. Jarmola, V. M. Acosta, K. Jensen, S. Chemerisov, and D. Budker, Temperature- and Magnetic-Field-Dependent Longitudinal Spin Relaxation in Nitrogen-Vacancy Ensembles in Diamond, *Phys. Rev. Lett.* **108**, 197601 (2012).
- [38] S. Krinner, S. Storz, P. Kurpiers, P. Magnard, J. Heinsoo, R. Keller, J. Lütföld, C. Eichler, and A. Wallraff, Engineering cryogenic setups for 100-qubit scale superconducting circuit systems, *EPJ Quantum Technol.* **6**, 2 (2019).
- [39] T. Nozaki, Y. Shiota, S. Miwa, S. Murakami, F. Bonell, S. Ishibashi, H. Kubota, K. Yakushiji, T. Saruya, A. Fukushima, *et al.*, Electric-field-induced ferromagnetic resonance excitation in an ultrathin ferromagnetic metal layer, *Nat. Phys.* **8**, 491 (2012).
- [40] J. Zhu, J. A. Katine, G. E. Rowlands, Y.-J. Chen, Z. Duan, J. G. Alzate, P. Upadhyaya, J. Langer, P. K. Amiri, K. L. Wang, and I. N. Krivorotov, Voltage-Induced Ferromagnetic Resonance in Magnetic Tunnel Junctions, *Phys. Rev. Lett.* **108**, 197203 (2012).
- [41] P. K. Amiri and K. L. Wang, Voltage-controlled magnetic anisotropy in spintronic devices, *SPIN* **02**, 1240002 (2012).
- [42] W.-G. Wang, M. Li, S. Hageman, and C. L. Chien, Electric-field-assisted switching in magnetic tunnel junctions, *Nat. Mater.* **11**, 64 (2012).
- [43] L. Liu, C.-F. Pai, Y. Li, H. W. Tseng, D. C. Ralph, and R. A. Buhrman, Spin-torque switching with the giant spin hall effect of tantalum, *Science* **336**, 555 (2012).
- [44] X. Liu, W. Zhang, M. J. Carter, and G. Xiao, Ferromagnetic resonance and damping properties of CoFeB thin films as free layers in MgO-based magnetic tunnel junctions, *J. Appl. Phys.* **110**, 033910 (2011).
- [45] G. Yu, P. Upadhyaya, Q. Shao, H. Wu, G. Yin, X. Li, C. He, W. Jiang, X. Han, P. K. Amiri, and K. L. Wang, Room-temperature skyrmion shift device for memory application, *Nano Lett.* **17**, 261 (2017).
- [46] W. G. Wang, C. Ni, G. X. Miao, C. Weiland, L. R. Shah, X. Fan, P. Parson, J. Jordan-sweet, X. M. Kou, Y. P. Zhang, *et al.*, Understanding tunneling magnetoresistance during thermal annealing in MgO-based junctions with CoFeB electrodes, *Phys. Rev. B* **81**, 144406 (2010).

- [47] M. J. H. Ku, T. X. Zhou, Q. Li, Y. J. Shin, J. K. Shi, C. Burch, L. E. Anderson, A. T. Pierce, Y. Xie, A. Hamo, *et al.*, Imaging viscous flow of the Dirac fluid in graphene, *Nature* **583**, 537 (2020).
- [48] T. Lenz, G. Chatzidrosos, Z. Wang, L. Bougas, Y. Dumeige, A. Wickenbrock, N. Kerber, J. Zázvorka, F. Kammerbauer, M. Kläui, *et al.*, Imaging Topological Spin Structures Using Light-Polarization and Magnetic Microscopy, *Phys. Rev. Appl.* **15**, 024040 (2021).
- [49] N. J. McLaughlin, H. Wang, M. Huang, E. Lee-Wong, L. Hu, H. Lu, G. Q. Yan, G. Gu, C. Wu, Y.-Z. You, and C. R. Du, Strong correlation between superconductivity and ferromagnetism in an Fe-chalcogenide superconductor, *Nano Lett.* **21**, 7277 (2021).
- [50] B. Rana and Y. Otani, Towards magnonic devices based on voltage-controlled magnetic anisotropy, *Commun. Phys.* **2**, 90 (2019).
- [51] C.-G. Duan, J. P. Velev, R. F. Sabirianov, Z. Zhu, J. Chu, S. S. Jaswal, and E. Y. Tsymbal, Surface Magnetoelectric Effect in Ferromagnetic Metal Films, *Phys. Rev. Lett.* **101**, 137201 (2008).
- [52] K. Nakamura, R. Shimabukuro, Y. Fujiwara, T. Akiyama, T. Ito, and A. J. Freeman, Giant Modification of the Magnetocrystalline Anisotropy in Transition-Metal Monolayers by an External Electric Field, *Phys. Rev. Lett.* **102**, 187201 (2009).
- [53] M. Tsujikawa and T. Oda, Finite Electric Field Effects in the Large Perpendicular Magnetic Anisotropy Surface Pt/Fe/Pt(001): A First-Principles Study, *Phys. Rev. Lett.* **102**, 247203 (2009).
- [54] S. Kanai, M. Gajek, D. C. Worledge, F. Matsukura, and H. Ohno, Electric field-induced ferromagnetic resonance in a CoFeB/MgO magnetic tunnel junction under dc bias voltages, *Appl. Phys. Lett.* **105**, 242409 (2014).
- [55] Y. Shiota, S. Miwa, S. Tamaru, T. Nozaki, H. Kubota, A. Fukushima, Y. Suzuki, and S. Yuasa, High-output microwave detector using voltage-induced ferromagnetic resonance, *Appl. Phys. Lett.* **105**, 192408 (2014).
- [56] L. Childress and R. Hanson, Diamond NV centers for quantum computing and quantum networks, *MRS Bull.* **38**, 134 (2013).
- [57] K. Watanabe, B. Jinna, S. Fukami, H. Sato, and H. Ohno, Shape anisotropy revisited in single-digit nanometer magnetic tunnel junctions, *Nat. Commun.* **9**, 663 (2018).
- [58] T. van der Sar, F. Casola, R. Walsworth, and A. Yacoby, Nanometre-scale probing of spin waves using single electron spins, *Nat. Commun.* **6**, 7886 (2015).
- [59] T. Song, Q.-C. Sun, E. Anderson, C. Wang, J. Qian, T. Taniguchi, K. Watanabe, M. A. McGuire, R. Stöhr, D. Xiao, *et al.*, Direct visualization of magnetic domains and moiré magnetism in twisted 2D magnets, *Science* **374**, 1140 (2021).
- [60] M. Pelliccione, A. Jenkins, P. Ovartchaiyapong, C. Reetz, E. Emmanouilidou, N. Ni, and A. C. Bleszynski Jayich, Scanned probe imaging of nanoscale magnetism at cryogenic temperatures with a single-spin quantum sensor, *Nat. Nanotechnol.* **11**, 700 (2016).
- [61] F. Oliveira, Ph.D. thesis, University of Stuttgart, 2017.
- [62] R. Hanson, V. V. Dobrovitski, A. E. Feiguin, O. Gywat, and D. D. Awschalom, Coherent dynamics of a single spin interacting with an adjustable spin bath, *Science* **320**, 352 (2008).
- [63] S. U. Jen, T. Y. Chou, and C. K. Lo, Impedance of nanometer thickness ferromagnetic Co₄₀Fe₄₀B₂₀ films, *Nanoscale Res. Lett.* **6**, 468 (2011).
- [64] A. Zangwill, *Modern Electrodynamics* (Cambridge University Press, Cambridge, 2013).